

# Nanoscale

Accepted Manuscript

This article can be cited before page numbers have been issued, to do this please use: J. Chen, Y. Zhao, W. Feng, Y. Guo, B. Tian and J. Jiang, *Nanoscale*, 2026, DOI: 10.1039/D5NR05332C.



This is an Accepted Manuscript, which has been through the Royal Society of Chemistry peer review process and has been accepted for publication.

Accepted Manuscripts are published online shortly after acceptance, before technical editing, formatting and proof reading. Using this free service, authors can make their results available to the community, in citable form, before we publish the edited article. We will replace this Accepted Manuscript with the edited and formatted Advance Article as soon as it is available.

You can find more information about Accepted Manuscripts in the [Information for Authors](#).

Please note that technical editing may introduce minor changes to the text and/or graphics, which may alter content. The journal's standard [Terms & Conditions](#) and the [Ethical guidelines](#) still apply. In no event shall the Royal Society of Chemistry be held responsible for any errors or omissions in this Accepted Manuscript or any consequences arising from the use of any information it contains.

# 1 Interface Carrier Transport in van der Waals 2 Heterostructures: Roles of Bubbles, Annealing, and Electric 3 Field Screening

4 Jianwei Chen<sup>1</sup>, Yike Zhao<sup>1</sup>, Wuwei Feng<sup>1</sup>, Yajie Guo<sup>2, 3\*</sup>, Bo Tian<sup>4\*</sup>, Jun Jiang<sup>5\*</sup>

5 1. School of Marine Engineering Equipment, Zhejiang Ocean University, Zhoushan, 316022,  
6 China

7 2. Institute of Wideband Gap Semiconductor Materials and Devices, Research Institute of Fudan  
8 University in Ningbo, Ningbo, 315336, China

9 3. College of Intelligent Robotics and Advanced Manufacturing, Fudan University, Shanghai,  
10 200433, China

11 4. Nanophotonics Research Centre, Shenzhen Key Laboratory of Micro-Scale Optical  
12 Information Technology, Institute of Microscale Optoelectronics & State Key Laboratory of  
13 Radio Frequency Heterogeneous Integration, Shenzhen University, Shenzhen, 518060, China

14 5. Zhejiang Province Engineering Research Center for Endoscope Instruments and Technology  
15 Development, Quzhou People's Hospital, The Quzhou Affiliated Hospital of Wenzhou Medical  
16 University, Quzhou, 324000, China

17 \*Corresponding author: [guoyajie@fudan.edu.cn](mailto:guoyajie@fudan.edu.cn) (Y Guo), [tianbo@szu.edu.cn](mailto:tianbo@szu.edu.cn) (Bo Tian),  
18 [jj1149777543@163.com](mailto:jj1149777543@163.com) (J Jiang)

## 19 ABSTRACT

20 Van der Waals (vdW) two-dimensional (2D) materials are pivotal for advancing high-  
21 performance electronic and optoelectronic devices in the post-Moore era. However, their practical  
22 performance is severely limited by interface quality, which poses a critical bottleneck. Herein, we  
23 systematically investigate the electrical response of vdW interfaces under electric fields, thermal  
24 annealing, and alternating current excitation, thereby establishing a theoretical basis and technical  
25 pathway for interface optimization. Specifically, using peak force tunneling amperemeter (TUNA)  
26 atomic force microscopy (AFM), we directly observe that interface bubbles impede interlayer  
27 carrier transport in vdW heterostructures. Furthermore, thermal annealing investigations reveal a  
28 non-monotonic modulation of the rectifying behavior in the heterostructure. Additionally, electric  
29 field distribution simulations provide insights into the mechanisms for the attenuation or screening  
30 of vertical electric fields across various vdW interfaces. Overall, this work offers a rigorous,



31 actionable framework integrating physical insights and application needs, with significant  
32 implications for precise interface design, optimized thermoelectric processing windows, and  
33 reliable integration of wafer-scale 2D material devices.

34 **KEYWORDS:** van der Waals two-dimensional materials, interface engineering, electric field,  
35 thermal annealing, rectifying behavior

## 36 1. INTRODUCTION

37 Van der Waals (vdW) two-dimensional (2D) materials, owing to their atomic-scale thickness,  
38 tunable bandgaps, strong light–matter interactions, and weak interlayer coupling<sup>[1–5]</sup>, have  
39 emerged as ideal candidates for next-generation electronics, optoelectronics, sensor, and quantum  
40 devices in the post-Moore era<sup>[6–9]</sup>. Their material-as-device structural advantage is particularly  
41 pronounced in applications such as heterogeneous integration, flexible electronics, and wafer-  
42 scale device fabrication<sup>[10–13]</sup>. However, interface quality hinders the transition of vdW 2D  
43 materials from laboratory prototypes to industrial-scale manufacturing. Unlike conventional  
44 semiconductors that form stable interfaces through strong covalent bonds, vdW materials rely on  
45 physical adsorption and weak interlayer interactions for stacking. As a result, their interfaces are  
46 highly susceptible to contamination from transfer residues, interface bubbles, surface impurities,  
47 and lattice mismatch<sup>[14–17]</sup>. Although these microscopic interface defects do not disrupt the crystal  
48 lattice itself, they profoundly influence carrier transport, contact resistance, band alignment, and  
49 device stability<sup>[18–20]</sup>, acting as an invisible killer that limits performance uniformity,  
50 manufacturing yield, and long-term reliability. As such, interface engineering constitutes a critical  
51 research focus for both fundamental studies and the industrialization of 2D materials.

52 Currently, research on vdW interfaces primarily centers on three key directions. First, the



53 influence of interface structure on device performance. Numerous studies have revealed how  
54 interface bubbles, polymer residues, interlayer twist angles, and wrinkles influence carrier  
55 mobility<sup>[21]</sup>, band structure<sup>[22]</sup>, interlayer coupling<sup>[23]</sup>, and photoluminescence properties<sup>[24, 25]</sup>. In  
56 vertical heterostructure device arrays, physical isolation at the interface can completely suppress  
57 interlayer charge transfer<sup>[19]</sup>, resulting in poor uniformity across the array. Second, the  
58 development of interface optimization strategies. Techniques such as thermal annealing<sup>[26, 27]</sup>,  
59 residue-free transfer<sup>[28–30]</sup>, and ultra-flat transfer<sup>[31, 32]</sup> are all pursued with the common goal of  
60 achieving atomically clean interfaces. Among these, thermal annealing has drawn particular  
61 interest because of its compatibility with silicon back-end-of-line (BEOL) processes. However,  
62 its narrow thermal processing window and reported side effects, such as atomic interdiffusion at  
63 elevated temperatures, present significant challenges<sup>[33–36]</sup>. Third, maintaining atomically flat  
64 contact interfaces over centimeter-scale or wafer-scale areas<sup>[37, 38]</sup>, suppressing interface stress-  
65 induced structural reconstruction, and achieving spatially uniform electrical performance<sup>[39–41]</sup>.  
66 Addressing these issues represents both a frontier in fundamental research and a critical milestone  
67 for industrial-scale manufacturing.

68 Although significant progress has been made in understanding the relationship between  
69 interfaces and device performance, existing studies still exhibit clear limitations. Most research  
70 has focused on the behavior of interfaces and surfaces in single vdW 2D materials under electrical  
71 characterization<sup>[21, 42–44]</sup>, with little systematic investigation into the co-evolution of stacked vdW  
72 interfaces under dynamic operating conditions, such as electric fields, thermal stress, or  
73 alternating current signals. In particular, at the heterostructure device level, there remains a lack  
74 of quantitative comparisons and mechanistic insights into how interface quality influences



75 electrical stability and functional retention. Moreover, while the distribution, attenuation, and  
76 screening behavior of vertical electric fields at the intrinsic, atomically sharp interfaces of pristine  
77 vdW materials have been studied<sup>[45, 46]</sup>, the corresponding behavior at artificially engineered  
78 interfaces formed during device fabrication has not been systematically explored. This knowledge  
79 gap severely hinders precise control over interface charge distribution and the rational design of  
80 band engineering strategies.

81 This work systematically investigates the electrical response and evolution of vdW  
82 heterostructure interfaces under various physical stimuli. First, we employ peak-force tunneling  
83 amperemeter (TUNA) atomic force microscopy (AFM) to visualize the distinct impacts of  
84 interface bubbles on interlayer carrier transport. Second, we apply controlled thermal annealing  
85 to reveal the non-monotonic evolution of rectifying characteristics. Finally, by integrating electric  
86 field distribution simulations, we systematically analyze the screening effects and field  
87 distribution characteristics across different types of interfaces. This study not only provides new  
88 insights into the intrinsic relationship between interface microstructure and macroscopic device  
89 performance but also delivers experimental evidence and practical guidance for optimizing  
90 interface engineering and enhancing reliability in wafer-scale 2D devices.

## 91 **2. EXPERIMENTAL METHODS**

### 92 **2.1 Fabrication and Characterization of vdW 2D Material Devices**

93 Few-layer MoS<sub>2</sub> and WSe<sub>2</sub> were exfoliated from bulk crystals via mechanical cleavage and  
94 precisely stacked using a dry-transfer technique to fabricate WSe<sub>2</sub>/MoS<sub>2</sub> heterostructure,  
95 respectively. Ti/Au (10 nm/100 nm) metal contacts were then deposited onto the devices using  
96 photolithography combined with electron-beam evaporation to form electrical contacts. To



97 characterize the electrical properties of surfaces and interfaces in the 2D material heterostructure,  
98 WSe<sub>2</sub>/MoS<sub>2</sub> devices were placed in an AFM system. Under peak force TUNA mode (fA-level  
99 current detection sensitivity, a noise floor below 100 fA, an amplifier bandwidth of 15 kHz, and  
100 a gain range of 10<sup>7</sup>–10<sup>10</sup> V/A), a probe bias of +3 V (positive polarity) was applied to the  
101 conductive AFM tip to acquire nanoscale maps of peak current distribution across the surface,  
102 focusing on vertical interlayer transport in the WSe<sub>2</sub>/MoS<sub>2</sub> stack. Conductive AFM measurements  
103 were performed in air using SCM-PIT-V2 probes (Pt/Ir-coated, nominal tip radius ≤25 nm), with  
104 a peak force setpoint of 20 nN and a scan rate of 0.5 Hz. To further investigate the impact of  
105 thermal treatment on interface properties, WSe<sub>2</sub>/MoS<sub>2</sub> heterostructure devices were annealed in a  
106 tube furnace under an argon/hydrogen (Ar/H<sub>2</sub>) mixed atmosphere (67% Ar and 33% H<sub>2</sub>, with a  
107 total flow rate of 450 sccm) at a pressure of 3 torr. The annealing was performed post-fabrication,  
108 after the deposition of Ti/Au metal contacts. Sequential annealing steps were carried out: the  
109 temperature was ramped up at 15 °C/min from room temperature to 300 °C, held for 2 hours, and  
110 then cooled naturally to room temperature. This was followed by a second annealing cycle,  
111 ramping up at 15 °C/min to 450 °C, held for 2 hours, and cooled naturally. After each annealing  
112 step, the direct current (DC) current–voltage characteristics of the devices were measured.

113 To evaluate rectification under dynamic conditions, alternating current (AC) characterization  
114 was performed on the same WSe<sub>2</sub>/MoS<sub>2</sub> heterostructure devices using a voltage-divider  
115 configuration. A function generator delivered a clean sinusoidal voltage with peak-to-peak  
116 amplitude ( $V_{pp}$ ) of 6 V and frequency of 200 Hz. The generator output impedance was set to 50  
117 Ω with corresponding termination. The device was connected in series with a fixed load resistor  
118 of 4.7 MΩ. The voltage appearing across this load resistor ( $V_{out}$ ) was acquired using one channel



119 of a digital storage oscilloscope. The input waveform was simultaneously monitored via a separate  
120 channel using the same probe configuration. All AC measurements were conducted at room  
121 temperature in ambient air. Critically, the excitation conditions, 6 V<sub>pp</sub> amplitude, 200 Hz  
122 frequency, 4.7 MΩ load, and probe configuration, were kept identical for the as-fabricated device  
123 and after each annealing step (300 °C and 450 °C), ensuring that any observed changes in output  
124 waveform shape and rectification quality arise solely from modifications to the heterostructure  
125 interface rather than variations in the measurement setup.

## 126 2.2 Electric Field Distribution Simulation at Interfaces of vdW 2D Materials

127 In this work, we adopt a simplified electrostatic model in COMSOL Multiphysics to  
128 investigate the spatial distribution of the effective electric field under an externally applied vertical  
129 electric field. While a fully atomistic description would require first-principles calculations, our  
130 framework approximates the strong intra-layer covalent bonding (S–Mo–S in MoS<sub>2</sub> and Se–W–  
131 Se in WSe<sub>2</sub>) by placing fixed positive and negative charge densities at discrete planes  
132 corresponding to the atomic positions within each monolayer. Specifically, each monolayer is  
133 modeled as a 0.67 nm thick slab (approximating the interlayer spacing in bulk TMDs). In  
134 COMSOL Multiphysics simulations, the charge distribution within 2D TMD layers is modeled as  
135 a uniform surface charge density ( $\sigma$ ), applied to infinitesimally thin boundary planes positioned  
136 at the atomic layers within the structural slab. Specifically, for an N-type MoS<sub>2</sub> layer, a positive  
137 surface charge density ( $\sigma_{\text{Mo}}$ ) is applied to the central plane (the Mo atomic layer), while negative  
138 surface charge densities ( $\sigma_{\text{S}}$ ) are applied at symmetric positions above and below (corresponding  
139 to the top and bottom S atomic layers, respectively). Conversely, for a P-type WSe<sub>2</sub> layer, an  
140 opposite charge polarity configuration is adopted: a negative surface charge density ( $\sigma_{\text{W}}$ ) is



141 applied to the central plane (the W atomic layer), and positive surface charge densities ( $\sigma_{\text{Se}}$ ) are  
142 applied at the positions of the Se atomic layers above and below. To ensure overall electrical  
143 neutrality for each material, the net charge within each unit cell is zero, satisfying the conditions  
144  $\sigma_{\text{Mo}}+2\sigma_{\text{S}}=0$  and  $\sigma_{\text{W}}+2\sigma_{\text{Se}}=0$ . The magnitude of these sheet charges is chosen to reproduce the  
145 known macroscopic dielectric constant of the material ( $\epsilon_r \approx 4$  for multilayer MoS<sub>2</sub> and similar for  
146 WSe<sub>2</sub>), calibrated such that the internal electric field oscillations and average screening match  
147 reported values from literature for pristine vdW layers. The interlayer regions (either vdW gap in  
148 homostructures or the tunable air gap emulating bubbles in heterostructures) are treated as vacuum  
149 ( $\epsilon_r = 1$ ) with zero charge density. By capturing the key features of our model, we avoid the need  
150 to impose complex boundary conditions. Although the entire structure is three-dimensional, the  
151 bubble is sufficiently large in the x–y plane. We can therefore approximate the bubble as infinitely  
152 extended when investigating the electric field distribution inside it. This allows the full  
153 three-dimensional structure to be studied using a one-dimensional model, in which the two  
154 directions perpendicular to the one-dimensional axis are treated as infinitely large by default in  
155 the software. This is equivalent to applying periodic boundary conditions in three-dimensional  
156 space.

157 This fixed-sheet-charge representation is appropriate and advantageous for the dielectric  
158 screening problem under consideration for several reasons. First, it captures the essential physics  
159 of polarization screening in layered vdW materials without requiring computationally intensive  
160 atomic-scale resolution: the discrete charge planes mimic the strong intra-layer dipoles and  
161 polarization response, leading to periodic oscillations of the electric field inside each monolayer  
162 (as observed in our results) and effective attenuation of the field across multiple layers, consistent



163 with macroscopic dielectric behavior. Second, this approach directly highlights the role of  
164 dielectric contrast (high- $\epsilon_r$  TMD vs. low- $\epsilon_r$  air/vacuum) in voltage division and field  
165 enhancement/dilution within bubbles, which is the key mechanism we aim to elucidate. Unlike  
166 purely macroscopic models that treat each layer as a uniform dielectric without internal structure,  
167 our method retains some microscopic character (layered charge separation) to better reproduce  
168 the non-monotonic field behavior in the air gap as its thickness varies from sub-nm to tens of nm.

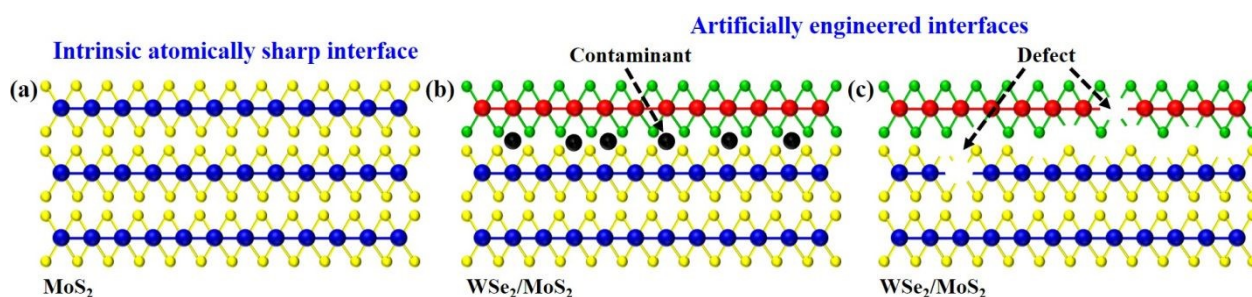
### 169 3. RESULTS

#### 170 3.1 Classification of Interfaces in vdW 2D Materials

171 Interfaces in vdW 2D materials can be broadly categorized into intrinsically atomically sharp  
172 interfaces (**Figure 1a**) and artificially engineered interfaces (**Figures 1b and 1c**). Intrinsic  
173 atomically sharp interfaces are typically obtained by mechanical exfoliation of bulk crystals and  
174 exhibit atomic-level flatness and exceptional cleanliness, serving as an ideal benchmark for  
175 evaluating the intrinsic performance of devices. In contrast, artificially engineered interfaces are  
176 formed during transfer, stacking, and micro/nanofabrication processes, which often introduce  
177 interface contaminants (**Figure 1b**) and structural defects (**Figure 1c**). Contaminants primarily  
178 originate from residues of transfer media, environmental adsorbates, or impurities introduced  
179 during processing atmospheres. Structural defects often arise from lattice imperfections inherent  
180 to chemical vapor deposition (CVD) growth or from localized damage induced by subsequent  
181 microfabrication steps. This work systematically investigates the evolution of electrical behavior  
182 in these distinct interfaces under the combined influence of electric and thermal fields. We focus  
183 on elucidating their differential impacts on key performance metrics, including carrier transport  
184 efficiency, rectification characteristics, and electrical stability. The findings aim to provide



185 theoretical insights and design guidelines for interface engineering toward high-performance and  
 186 highly reliable vdW 2D material devices.



187  
 188 **Figure 1** Classification of interfaces in vdW 2D materials. (a) Intrinsic atomically sharp interfaces.

189 (b, c) Artificially engineered interfaces, including interface contaminants and interface defects.

### 190 3.2 Correlation between Interface Quality and Surface Peak Current in vdW 2D Material

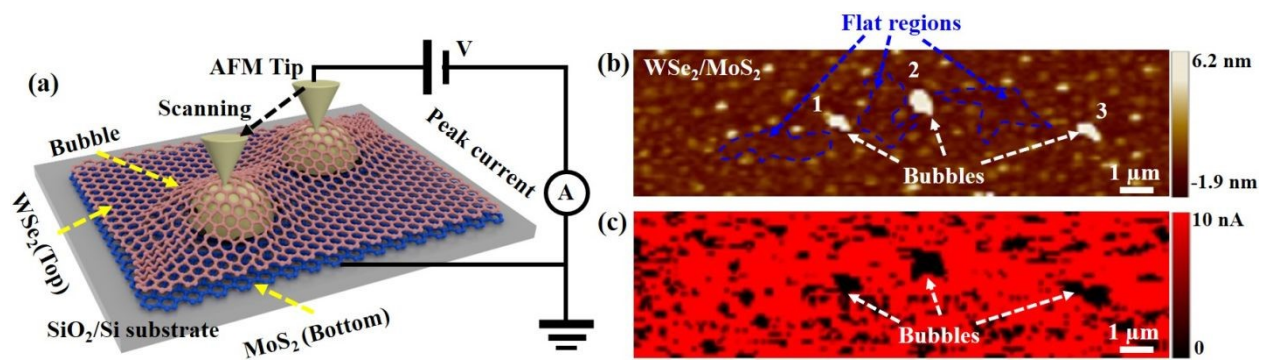
#### 191 Heterostructure

192 WSe<sub>2</sub>/MoS<sub>2</sub> vdW heterostructure devices containing interface bubbles were fabricated on  
 193 SiO<sub>2</sub>/Si substrate using standard photolithography patterning followed by metal evaporation and  
 194 lift-off processes. These bubbles, unintentionally introduced during mechanical exfoliation and  
 195 dry-transfer stacking of the 2D flakes, serve as natural testbeds for probing the sensitivity of  
 196 interlayer charge transport to nanoscale interface imperfections. To quantitatively assess their  
 197 impact, the devices were characterized using conductive AFM operated in peak force TUNA  
 198 mode, which enables simultaneous acquisition of topographical and nanoscale current maps with  
 199 high spatial resolution and minimal sample damage.

200 In the measurement configuration schematically depicted in Figure 2a, which illustrates the  
 201 electrical setup with tip bias on WSe<sub>2</sub> and grounding on MoS<sub>2</sub> to probe vertical transport, a +3 V  
 202 bias (positive polarity) was applied to the conductive AFM tip in contact with the top WSe<sub>2</sub> layer,  
 203 while the underlying MoS<sub>2</sub> flake was electrically grounded through a metal contact. The resulting  
 204 AFM topography (**Figure 2b**) clearly reveals three well-defined interface bubbles labeled 1, 2,



205 and 3, with vertical heights of 24.5 nm, 26.4 nm, and 29.2 nm, respectively. Critically, the  
 206 corresponding peak current map (**Figure 2c**), acquired concurrently under identical conditions,  
 207 shows a complete absence of measurable current (0 pA) across all three bubble regions. In stark  
 208 contrast, the surrounding flat regions exhibit robust and spatially uniform conduction, confirming  
 209 that the loss of current is directly correlated with the presence of the bubbles rather than material  
 210 degradation or contact failure.



211  
 212 **Figure 2** Surface current distribution characteristics of vdW 2D material heterostructures. (a)  
 213 Schematic illustration of surface current measurement on a vdW heterostructure with interface  
 214 bubbles. (b, c) AFM topography and corresponding surface peak current map of a WSe<sub>2</sub>/MoS<sub>2</sub>  
 215 heterostructure.

216 While a monolayer of WSe<sub>2</sub> or MoS<sub>2</sub> is only approximately 0.7 nm thick, bubble-induced  
 217 gaps reaching tens of nanometers in height create separations over 30 to 40 times larger. These  
 218 distances (24.5–29.2 nm) far exceed the decay length of electronic wavefunctions in 2D  
 219 semiconductors, effectively eliminating interlayer orbital hybridization. To quantify this, consider  
 220 a simple rectangular barrier tunneling model where the transmission probability  $P$  scales as  $\exp(-$   
 221  $2\kappa d)$ , with decay constant  $\kappa \approx \sqrt{2m\phi}/\hbar$ . Using reasonable parameters for TMD-air interfaces  
 222 (effective mass  $m \approx$  electron mass, barrier height  $\phi \approx 4$  eV based on work functions),  $\kappa \approx 10$  nm<sup>-1</sup>.  
 223 Assuming  $\Delta d$  corresponds to a characteristic bubble height of 26.4 nm, the calculation yields



224  $\exp(-\approx 528) \approx 10^{-229}$ , corresponding to a suppression of the tunneling probability by more than 200  
225 orders of magnitude. This estimate, while approximate and neglecting factors like effective mass  
226 renormalization or band structure details, confirms the near-total transport suppression observed  
227 in the current maps. Consequently, the vertical current is nearly extinguished in these regions, this  
228 complete suppression of vertical current in bubble regions suggests that the large separations  
229 strongly inhibit interlayer orbital overlap and tunneling. Achieving atomically clean, conformal,  
230 and flat interfaces throughout the heterostructure stack is therefore not merely an ideal but an  
231 absolute prerequisite for unlocking the intrinsic electronic and optoelectronic properties of 2D  
232 materials.

### 233 **3.3 Correlation between Interface Quality and Electrical Properties of vdW 2D Material**

#### 234 **Heterostructure under Thermal Annealing Treatment**

235 Thermal annealing is a well-established and effective technique for cleaning surfaces and  
236 interfaces in vdW 2D heterostructures, and it is fully compatible with BEOL processes in silicon-  
237 based integrated circuit fabrication<sup>[26, 27, 38]</sup>. In this work, WSe<sub>2</sub>/MoS<sub>2</sub> vertical heterostructure  
238 diodes were fabricated via standard photolithography and metal deposition, followed by post-  
239 fabrication annealing in a tube furnace under an Ar/H<sub>2</sub> ambient at varying temperatures.

240 Current–voltage characteristics were systematically measured at three stages: as-fabricated  
241 (before annealing), after annealing at 300 °C, and after annealing at 450 °C, as summarized in  
242 Figure 3a, with each based on a single forward–reverse sweep from -3 V to +3 V. The as-fabricated  
243 device exhibited poor electrical performance, delivering only 0.05 nA at +3 V with a modest  
244 rectification ratio of approximately 5, defined as the ratio of forward current  $I(+3\text{ V})$  to the  
245 absolute reverse current  $|I(-3\text{ V})|$  without averaging over multiple sweeps. Upon annealing at



246 300 °C, the forward current surged by over four orders of magnitude to 758.7 nA at +3 V, and the  
247 rectification ratio improved dramatically to 85 using the same calculation, clear hallmarks of a  
248 functional p–n junction with strong forward conduction and effective reverse blocking. This  
249 marked enhancement is attributed to the thermal removal of residual polymers from the transfer  
250 process and potential migration and coalescence of interface bubbles, hypothesized based on  
251 improved carrier transport and prior reports<sup>[26,27]</sup>, which could collectively yield a cleaner, more  
252 intimate, and atomically flat vdW interface.

253 However, further increasing the annealing temperature to 450 °C led to significant  
254 performance degradation: the current at +3 V dropped to 234 nA, and the rectification ratio  
255 collapsed to just 1.4. This deterioration is consistent with prior reports of thermally activated  
256 atomic interdiffusion in heterostructures<sup>[33–36]</sup>, though our attribution relies on electrical evidence  
257 rather than direct materials characterization. We hypothesize two interrelated potential  
258 mechanisms: first, interdiffusion of chalcogen atoms (Se and S) across the WSe<sub>2</sub>/MoS<sub>2</sub> interface,  
259 blurring the p–n junction; second, diffusion of metal atoms, notably Ti from the contacts, into the  
260 semiconductor channels, introducing defects. To validate the above assertion, future work should  
261 employ characterization techniques to visualize interfacial intermixing or profile elemental  
262 distributions. Together, these processes reconstruct the interface energy landscape, suppress the  
263 built-in electric field, and render carrier transport nearly symmetric, effectively transforming the  
264 diode into an ohmic-like or quasi-homogeneous junction. While these single-sweep results  
265 highlight clear trends, repeat I–V sweeps (at least two per condition) would be valuable in future  
266 studies to address potential hysteresis, such as differences between forward and reverse scans due  
267 to trapping, or stability issues, ensuring the observed degradation is reproducible and not sweep-



268 dependent.

269 To further confirm the evolution of junction asymmetry observed in DC measurements, AC  
270 rectification tests were performed under identical excitation conditions as detailed in Section 2.1.  
271 A 6 V peak-to-peak, 200 Hz sinusoidal input was applied across the series combination of the  
272 heterostructure diode and a 4.7 M $\Omega$  load resistor (**Figure 3b**). The voltage developed across the  
273 load ( $V_{\text{out}}$ ) and the input waveform were recorded concurrently on the oscilloscope. As shown in  
274 **Figure 3c**, the device annealed at 300 °C produced a clear half-wave rectified output, whereas the  
275 waveform after 450 °C annealing closely followed the input sinusoid, indicating near-complete  
276 loss of rectifying behavior.

277 These results underscore a critical trade-off in thermal processing of 2D heterostructures.  
278 Moderate annealing, such as at 300 °C, optimizes interface quality and unlocks high-performance  
279 diode behavior, whereas excessive temperatures may trigger detrimental interface intermixing that  
280 irreversibly degrades electronic functionality. Therefore, precise control of annealing parameters,  
281 particularly temperature and ambient atmosphere, is essential for harnessing the full potential of  
282 vdW heterostructures in next-generation electronic and optoelectronic applications.

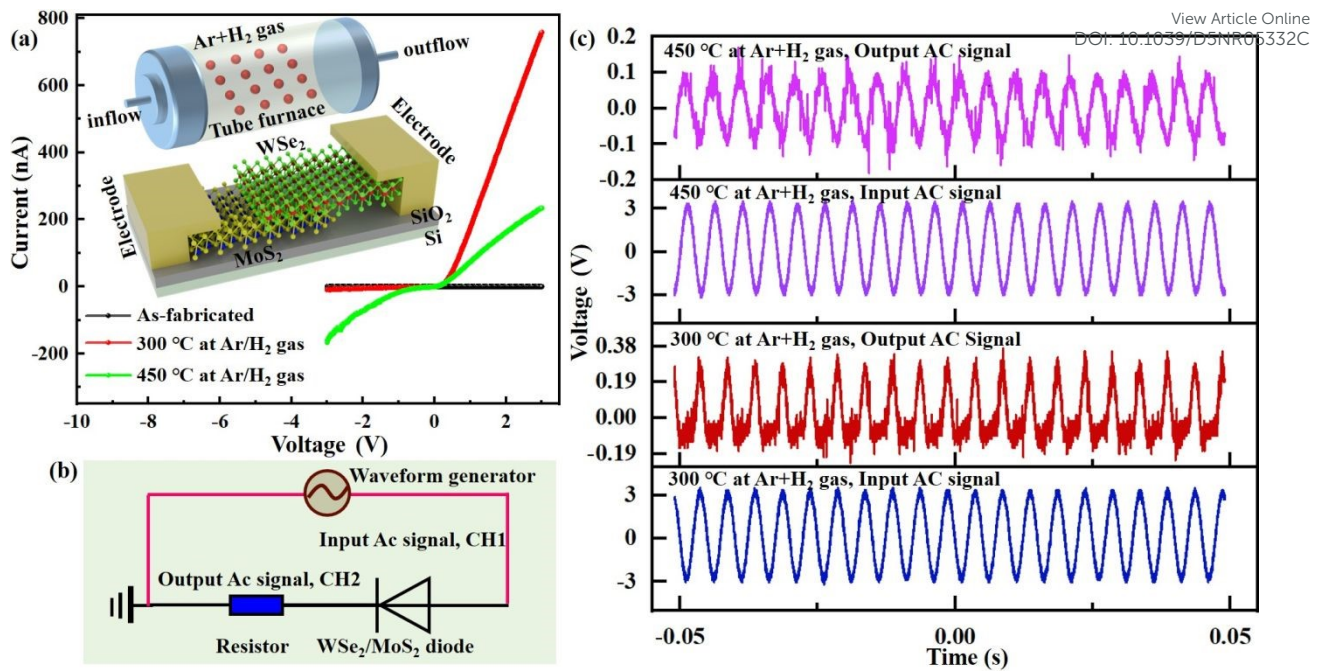


**Figure 3** Thermal annealing induced interface evolution in WSe<sub>2</sub>/MoS<sub>2</sub> heterostructure and its impact on rectification behavior. (a) Current–Voltage characteristics measured after annealing at different temperatures. The upper inset presents a schematic of the annealing process in a tube furnace, while the lower inset depicts the structural layout of the WSe<sub>2</sub>/MoS<sub>2</sub> device. (b) Circuit configuration for AC signal testing of the heterostructure diode. (c) Output signal waveforms recorded under identical sinusoidal input conditions, highlighting the pronounced degradation of rectification performance after high-temperature annealing.

### 3.4 Electric Field Distribution at Interfaces of vdW 2D Materials

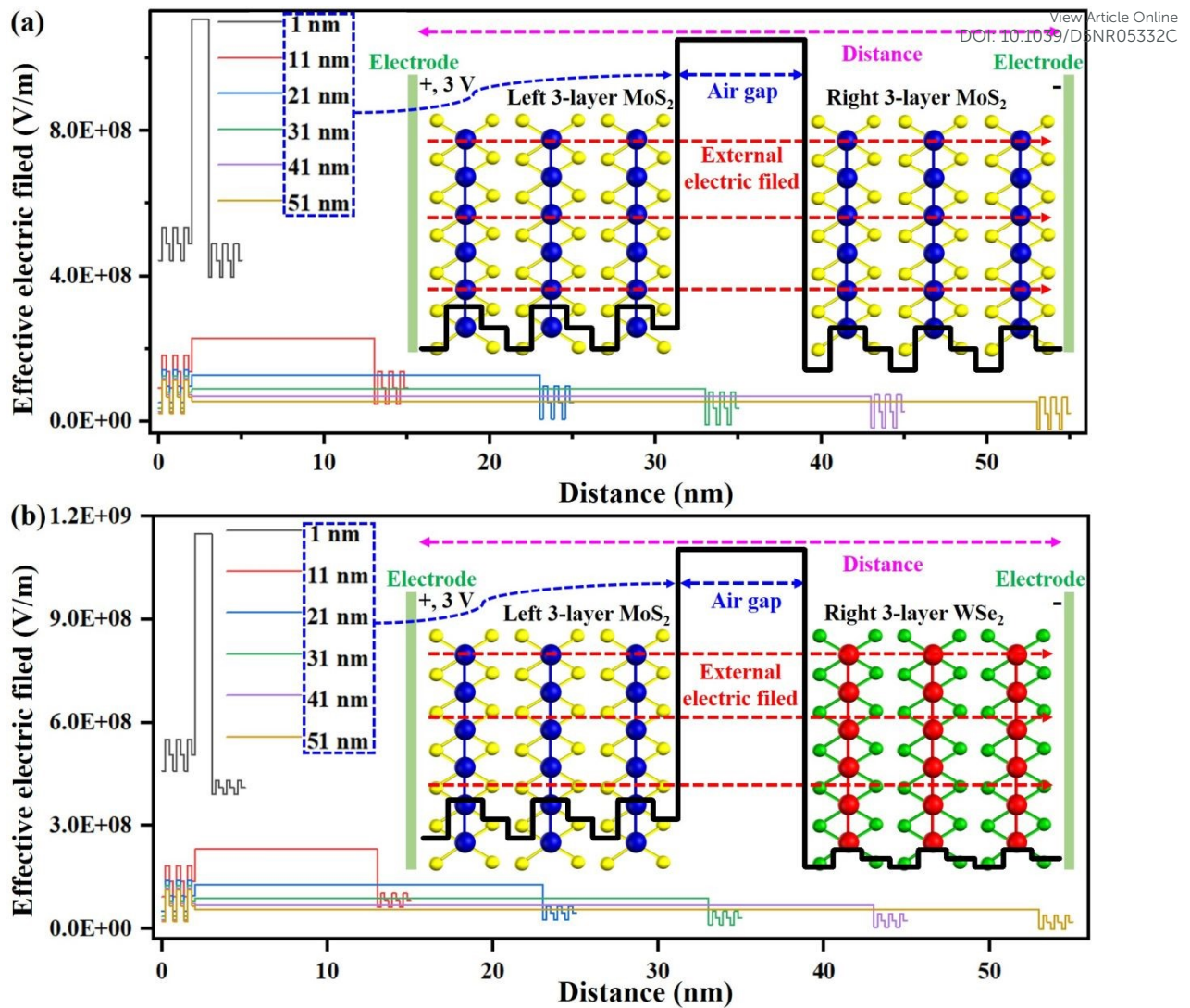
**Figure 4** presents a high-precision electrostatic model developed using COMSOL Multiphysics to investigate how the size of interface bubbles influences the spatial distribution of the effective electric field in vertically stacked vdW 2D heterostructures. In contrast to existing theoretical studies in the literature<sup>[45, 46]</sup>, which typically focus on ideal, defect-free, single-component systems such as pristine MoS<sub>2</sub> or graphene, our work innovatively introduces a tunable air gap to emulate the interface bubbles commonly present in real devices. We investigated the MoS<sub>2</sub>/MoS<sub>2</sub> homostructure and the WSe<sub>2</sub>/MoS<sub>2</sub> heterostructure, respectively. In our model,



299 positive and negative charges are fixed at their respective atomic lattice sites (S–Mo–S or Se–W  
300 Se), and each monolayer is assigned a thickness of 0.67 nm, enabling the macroscopic continuum  
301 framework to effectively capture atomic-scale charge polarization characteristics.

302 In the MoS<sub>2</sub>/MoS<sub>2</sub> homostructure (**Figure 4a**), under an externally applied vertical electric  
303 field, the effective electric field within the air gap exhibits pronounced size dependence. When  
304 the gap is extremely small (for example, 1 nm), the electric field in the gap is significantly higher  
305 than the average field inside the adjacent MoS<sub>2</sub> layers. As the gap widens, this field gradually  
306 decreases and, beyond a transition gap thickness of approximately 41 nm, drops below the field  
307 strength (Mo atom) inside the MoS<sub>2</sub> layers on either side. This behavior can be understood through  
308 dielectric voltage division. MoS<sub>2</sub> possesses a relatively high relative permittivity ( $\epsilon_r \approx 4$ ), whereas  
309 air has a much lower one ( $\epsilon_r \approx 1$ ), so the entire structure can be viewed as a series capacitor  
310 network composed of high- $\epsilon_r$  (MoS<sub>2</sub>) and low- $\epsilon_r$  (air) layers. According to basic electrostatics,  
311 under fixed free-charge conditions, the electric field  $E$  is inversely proportional to the dielectric  
312 constant  $\epsilon$ , but also depends on the layer thickness  $d$  ( $E = \Delta V/d$ ). When the air gap is ultrathin, its  
313 small thickness dominates over its low permittivity, resulting in an exceptionally high potential  
314 gradient, that is, a strong electric field, across the gap. As the gap widens, the air layer  
315 accommodates most of the applied voltage drop; however, because its thickness simultaneously  
316 increases, the electric field intensity actually diminishes. Once the gap exceeds approximately 41  
317 nm, the air layer becomes the dominant voltage divider, and its electric field becomes significantly  
318 diluted. Meanwhile, the internal effective field in the MoS<sub>2</sub> layers is further suppressed by their  
319 intrinsic polarization screening. Consequently, the field in the air gap eventually falls below that  
320 inside the MoS<sub>2</sub> layers. This entire process is driven purely by geometric dimensions and dielectric  
321 contrast, without involving built-in fields or band engineering, clearly illustrating the fundamental  
322 physical picture in vdW materials: thickness dictates screening capability.





323

324

325

326

327

328

329

330

331

332

333

**Figure 4** Effective electric field distribution at vdW 2D material interfaces. (a) Spatial distribution of the effective electric field in a MoS<sub>2</sub>/MoS<sub>2</sub> homostructure under an externally applied vertical electric field, for air gap thicknesses ranging from 1 to 51 nm (discrete preset values). The inset illustrates the localization of charges within the S–Mo–S atomic layers. The electric field inside MoS<sub>2</sub> exhibits periodic oscillations, while the field in the air gap shows a non-monotonic evolution with increasing gap thickness. (b) Spatial distribution of the effective electric field in a WSe<sub>2</sub>/MoS<sub>2</sub> heterostructure under an externally applied vertical electric field, for air gap thicknesses from 1 to 51 nm. The inset illustrates the localization of charges within the Se–W–Se atomic layers. Both MoS<sub>2</sub> and WSe<sub>2</sub> display periodic field oscillations internally, while the electric field in the air gap again exhibits a non-monotonic dependence on the gap size.



334 In contrast, the WSe<sub>2</sub>/MoS<sub>2</sub> heterostructure exhibits a distinctly different evolution of the  
335 electric field (**Figure 4b**). Although the air-gap field is also initially high for small gaps, as the  
336 gap increases beyond approximately 21 nm, the field continues to decrease but remains higher  
337 than the field (W atom) inside the right WSe<sub>2</sub> layer, even as it drops below that in the left MoS<sub>2</sub>  
338 layer. This difference is consistent with the presence of a built-in electric field arising from band  
339 alignment mismatch between the two materials. This built-in field vectorially superposes with the  
340 externally applied field: in the WSe<sub>2</sub> region, the two fields oppose each other, further suppressing  
341 the effective internal field, whereas in the MoS<sub>2</sub> region, they align, leading to a relatively enhanced  
342 field. As a result, even as the air gap thickens and its own field weakens, the electric field in the  
343 WSe<sub>2</sub> region remains pinned at a low baseline level, preventing the air-gap field from ever falling  
344 below it. In realistic heterostructures containing interface bubbles, our results quantitatively reveal  
345 how band engineering, via the built-in field, can actively modulate the macroscopic electric field  
346 distribution. This provides a novel physical mechanism and an additional design degree of  
347 freedom for developing next-generation electric-field-sensitive devices, such as asymmetric  
348 tunneling transistors, photodetectors, and reconfigurable logic units.

349 While the present simulations provide valuable insights into the role of bubble height in  
350 modulating vertical electric field distribution via dielectric contrast and geometry, several  
351 simplifications should be acknowledged. First, the interlayer air gap is treated as vacuum ( $\epsilon_r = 1$ )  
352 with no trapped residues or adsorbates. In practice, many interface bubbles contain residual  
353 transfer media, water vapor, or organic contaminants that elevate the local permittivity (potentially  
354  $\epsilon_r = 2-4$ ), which would reduce the dielectric contrast with the surrounding TMD layers ( $\epsilon_r \approx 4$ )  
355 and thereby weaken the pronounced field enhancement observed for small gaps and the rapid field  
356 dilution for larger gaps. In future investigations, parametric sweep analysis of the gap permittivity  
357 should be performed to demonstrate how the conclusions would be affected when the gap medium  
358 deviates from vacuum-like characteristics.

359 Furthermore, although the model effectively elucidates dielectric voltage division and built-in field effects, it is oversimplified and neglects key quantum aspects significant in 2D systems. View Article Online  
DOI: 10.1039/D5NR05332C

360 in field effects, it is oversimplified and neglects key quantum aspects significant in 2D systems.

361 For instance, quantum capacitance arising from the density of states in ultrathin layers is omitted,

362 potentially underestimating field screening at low biases. Similarly, layer-dependent dielectric

363 screening, where effective  $\epsilon_r$  varies with thickness due to electronic polarization, is not considered,

364 as our homogeneous assumption treats multilayers uniformly. These limitations stem from the

365 simplified electrostatic model, which prioritizes macroscopic insights over ab initio accuracy, and

366 could be addressed in future work with more detailed boundary conditions, adaptive meshing, and

367 hybrid quantum-classical solvers.

#### 368 4. CONCLUSIONS

369 This study highlights the pivotal role of interface quality in vdW 2D heterostructures as a

370 fundamental bottleneck that constrains the performance of next-generation electronic and

371 optoelectronic devices. To address the interface challenges impeding wafer-scale integration in

372 the post-Moore era, the authors systematically probe the electrical responses and dynamic

373 evolution of vdW interfaces under realistic operating conditions, including applied electric fields,

374 thermal annealing, and AC excitation. Using peak force conductive AFM, they directly image

375 interface bubbles and demonstrate their pronounced suppression of interlayer carrier transport.

376 Thermal annealing experiments reveal a non-monotonic dependence of rectification behavior on

377 annealing temperature. Moreover, by combining experimental insights with electric field

378 distribution simulations, the study elucidates how distinct interface types differentially attenuate

379 or screen vertical electric fields. Beyond advancing the fundamental understanding of interface

380 physics in vdW systems, this work establishes a robust, theory-informed yet practically oriented

381 framework for precision interface engineering, rational design of thermal–electrical processing

382 windows, and high-yield, reliable integration of wafer-scale 2D material devices.

### 383 **AUTHORS CONTRIBUTIONS**

384 Jianwei Chen and Yajie Guo conceived the idea and initiated the present study. Yajie Guo, Yike  
385 Zhao, and Bo Tian carried out the main experiments. Wuwei Feng offered suggestion in analyzing  
386 the data. Yike Zhao and Bo Tian carried out the simulation. Jianwei Chen, Yajie Guo, and Jun  
387 Jiang wrote the manuscript.

### 388 **DECLARATION**

389 The authors declare no competing financial interest.

### 390 **ACKNOWLEDGEMENT**

391 This work was supported by the Research Initiation Grant for Newly Recruited Faculty Zhejiang  
392 Ocean University (JX6311043025).

### 393 **REFERENCES**

- 394 [1] Y. Liu, N. O. Weiss, X. Duan, H. C. Cheng, Y. Huang, X. Duan, Van der Waals  
395 heterostructures and devices, *Nat. Mater.*, 2016, **1**, 1–17.
- 396 [2] A. Garcia-Ruiz, M. H. Liu, Twisted bilayer MoS<sub>2</sub> under electric fields: a system with tunable  
397 symmetry, *Nano Lett.*, 2024, **24**, 16317–16324.
- 398 [3] T. Guo, S. Chandra, A. Dasgupta, M. W. Shabbir, A. Biswas, D. Chanda, Spectrally tunable  
399 ultrafast long wave infrared detection at room temperature, *Nano Lett.*, 2024, **24**, 14678–  
400 14685.
- 401 [4] M. Chen, Y. Wang, Z. Zhao, Monolithic metamaterial-integrated graphene terahertz  
402 photodetector with wavelength and polarization selectivity, *ACS Nano*, 2022, **16**, 17263–  
403 17273.
- 404 [5] Y. Yang, X. Wang, S. C. Liu, Z. Li, Z. Sun, C. Hu, D. J. Xue, G. Zhang, J. S. Hu, Weak  
405 Interlayer Interaction in 2D Anisotropic GeSe<sub>2</sub>, *Adv. Sci.*, 2019, **6**, 1801810.
- 406 [6] L. Sun, Y. Zhang, G. Han, G. Hwang, J. Jiang, B. Joo, K. Watanabe, T. Taniguchi, Y. M.  
407 Kim, W. J. Yu, B. S. Kong, R. Zhao, H. Yang, Self-selective van der Waals heterostructures



- 408 for large scale memory array, *Nat. Commun.*, 2019, **10**, 3161.
- 409 [7] X. Huang, C. Liu, Z. Tang, S. Zeng, S. Wang, P. Zhou, An ultrafast bipolar flash memory  
410 for self-activated in-memory computing, *Nat. Nanotechnol.*, 2023, **18**, 486–492.
- 411 [8] F. Wang, F. Hu, M. Dai, S. Zhu, F. Sun, R. Duan, C. Wang, J. Han, W. Deng, W. Chen, M.  
412 Ye, S. Han, B. Qiang, Y. Jin, Y. Chua, N. Chi, S. Yu, D. Nam, S. H. Chae, Z. Liu, Q. J.  
413 Wang, A two-dimensional mid-infrared optoelectronic retina enabling simultaneous  
414 perception and encoding, *Nat. Commun.*, 2023, **14**, 1938.
- 415 [9] L. Loh, J. Wang, M. Grzeszczyk, M. Koperski, G. Eda, Towards quantum light-emitting  
416 devices based on van der Waals materials, *Nat. Rev. Electr. Eng.*, 2024, **1**, 815–829.
- 417 [10] M. Ao, X. Zhou, X. Kong, S. Gou, S. Chen, X. Dong, Y. Zhu, Q. Sun, Z. Zhang, J. Zhang,  
418 Q. Zhang, Y. Hu, C. Sheng, K. Wang, S. Wang, J. Wan, J. Han, W. Bao, P. Zhou, A RISC-  
419 V 32-bit microprocessor based on two-dimensional semiconductors, *Nature*, 2025, **640**, 654–  
420 661.
- 421 [11] A. T. Hoang, L. Hu, A. K. Katiyar, J. H. Ahn, Two-dimensional layered materials and  
422 heterostructures for flexible electronics, *Matter*, 2022, **5**, 4116–4132.
- 423 [12] Y. Peng, C. Cui, L. Li, Y. Wang, Q. Wang, J. Tian, Z. Huang, B. Huang, Y. Zhang, X. Li, J.  
424 Tang, Y. Chu, W. Yang, D. Shi, L. Du, N. Li, G. Zhang, Medium-scale flexible integrated  
425 circuits based on 2D semiconductors, *Nat. Commun.*, 2024, **15**, 10833.
- 426 [13] X. Yang, J. Li, R. Song, B. Zhao, J. Tang, L. Kong, H. Huang, Z. Zhang, L. Liao, Y. Liu, X.  
427 Duan, X. Duan, Highly reproducible van der Waals integration of two-dimensional  
428 electronics on the wafer scale, *Nat. Nanotechnol.*, 2023, **18**, 471–478.
- 429 [14] R. Hu, J. Song, W. Huang, A. N. Zhou, J. L. Lin, Y. Cao, S. Hu, Controlling interfacial  
430 adhesion during the transfer of large-area 2D materials: mechanisms, strategies, and research  
431 advances, *New Carbon Mater.*, 2025, **40**, 553–583.
- 432 [15] X. Liu, K. Xing, C. S. Tang, S. Sun, P. Chen, D. C. Qi, M. B. H. Breese, M. S. Fuhrer, A. T.  
433 S. Wee, X. Yin, Contact resistance and interfacial engineering: Advances in high-  
434 performance 2D-TMD based devices, *Prog. Mater. Sci.*, 2025, **148**, 101390.
- 435 [16] I. Gasparutti, S. H. Song, M. Neuman, X. Wei, K. Watanabe, T. Taniguchi, Y. L. Lee, How  
436 Clean is clean? Recipes for van der Waals heterostructure cleanliness assessment, *ACS Nano*,  
437 2020, **12**, 7701–7709.

View Article Online  
DOI: 10.1039/D5NR05332C



- 438 [17] H. S. Yoon, J. Oh, J. Y. Park, J. Kang, J. Kwon, T. Cusati, G. Fiori, G. Iannaccone, A.  
439 Fortunelli, V. O. Ozcelik, G. H. Lee, T. Low, S. C. Jun, Phonon-assisted carrier transport  
440 through a lattice-mismatched interface, *NPG Asia Mater.*, 2019, **11**, 14.
- 441 [18] S. J. Haigh, A. Gholinia, R. Jalil, S. Romani, L. Britnell, D. C. Elias, K. S. Novoselov, L. A.  
442 Ponomarenko, A. K. Geim, R. Gorbachev, Cross-sectional imaging of individual layers and  
443 buried interfaces of graphene-based heterostructures and superlattices, *Nat. Mater.*, 2012, **11**,  
444 764–767.
- 445 [19] B. Vasić, U. Ralević, S. Aškračić, D. Čapeta, M. Kralj, Correlation between morphology and  
446 local mechanical and electrical properties of van der Waals heterostructures, *Nanotechnology*,  
447 2022, **33**, 155707.
- 448 [20] W. Fan, H. Yan, H. Li, X. Wang, L. Tong, C. Su, Z. Zhang, X. Chen, Q. Wang, S. Yin,  
449 Multifunction realization in MoS<sub>2</sub>/WS<sub>2</sub>/h-BN heterojunction: Integrated self-powered high-  
450 performance photodetection, visualization, nonvolatile memory, and synaptic simulation,  
451 *Nano Energy*, 2024, **128**, 109900.
- 452 [21] N. Leconte, H. Kim, H. J. Kim, D. H. Ha, K. Watanabe, T. Taniguchi, J. Jung, S. Jung,  
453 Graphene bubbles and their role in graphene quantum transport, *Nanoscale*, 2017, **9**, 6041.
- 454 [22] W. Wang, L. Zhou, S. Hu, K. S. Novoselov, Y. Cao, Visualizing piezoelectricity on 2D  
455 crystals nanobubbles, *Adv. Funct Mater.*, 2021, **31**, 2005053.
- 456 [23] R. Ai, X. Cui, Y. Li, X. Zhuo, Local strain engineering of two-dimensional transition metal  
457 dichalcogenides towards quantum emitters, *Nano-Micro Lett.*, 2025, **17**, 104.
- 458 [24] A. V. Tyurnina, D. A. Bandurin, E. Khestanova, V. G. Kravets, M. Koperski, F. Guinea, A.  
459 N. Grigorenko, A. K. Geim, I. V. Grigorieva, Strained bubbles in van der Waals  
460 heterostructures as local emitters of photoluminescence with adjustable wavelength, *ACS*  
461 *Photonics*, 2019, **6**, 516–524.
- 462 [25] Y. Chen, Y. Wang, W. Shen, M. Wu, B. Li, Q. Zhang, S. Liu, C. Hu, S. Yang, Y. Gao, C.  
463 Jiang, Strain and interference synergistically modulated optical and electrical properties in  
464 ReS<sub>2</sub>/Graphene heterojunction bubbles, *ACS Nano*, 2022, **16**, 16271–16280.
- 465 [26] L. Zhou, C. Ge, H. Yang, Y. Sun, J. Zhang, A high-pressure enhanced coupling effect  
466 between graphene electrical contacts and two-dimensional materials thereby improving the



- 467 performance of their constituent FET devices, *J. Mater. Chem. C*, 2019, **7**, 15171.
- 468 [27] T. Uwanno, Y. Hattori, T. Taniguchi, K. Watanabe, K. Nagashio, Fully dry PMMA transfer  
469 of graphene on h-BN using a heating/cooling system, *2D Mater.*, 2015, **2**, 041002.
- 470 [28] W. Wang, N. Clark, M. Hamer, A. Carl, E. Tovari, S. Sullivan-Allsop, E. Tillotson, Y. Gao,  
471 H. de Latour, F. Selles, J. Howarth, E. G. Castanon, M. Zhou, H. Bai, X. Li, A. Weston, K.  
472 Watanabe, T. Taniguchi, C. Mattevi, T. H. Bointon, P. V. Wiper, A. J. Strudwick, L. A.  
473 Ponomarenko, A. V. Kretinin, R. Gorbachev, Clean assembly of van der Waals  
474 heterostructures using silicon nitride membranes, *Nat. Electron.*, 2023, **6**, 981–990.
- 475 [29] M. Lee, C. Kim, S. Y. Kwon, K. Lee, G. Kwak, H. Lim, J. H. Seol, Residue-free fabrication  
476 of 2D materials using van der Waals interactions, *Adv. Mater.*, 2025, **37**, 2418669.
- 477 [30] S. Wen, S. Zhou, H. Chen, Y. Gong, L. Kong, Y. Yin, C. Lan, C. Li, Y. Li, Contamination-  
478 free assembly of two-dimensional van der Waals heterostructures toward high-performance  
479 electronics and optoelectronics, *Appl. Mater. Today*, 2025, **43**, 102657.
- 480 [31] X. Gao, L. Zheng, F. Luo, J. Qian, J. Wang, M. Yan, W. Wang, Q. Wu, J. Tang, Y. Cao, C.  
481 Tan, J. Tang, M. Zhu, Y. Wang, Y. Li, L. Sun, G. Gao, J. Yin, L. Lin, Z. Liu, S. Qin, H.  
482 Peng, Integrated wafer-scale ultra-flat graphene by gradient surface energy modulation, *Nat.*  
483 *Commun.*, 2022, **13**, 5410.
- 484 [32] Y. Zhao, Y. Song, Z. Hu, W. Wang, Z. Chang, Y. Zhang, Q. Lu, H. Wu, J. Liao, W. Zou, X.  
485 Gao, K. Jia, L. Zhuo, J. Hu, Q. Xie, R. Zhang, X. Wang, L. Sun, F. Li, L. Zheng, M. Wang,  
486 J. Yang, B. Mao, T. Fang, F. Wang, H. Zhong, W. Liu, R. Yan, J. Yin, Y. Zhang, Y. Wei, H.  
487 Peng, L. Lin, Z. Liu, Large-area transfer of two-dimensional materials free of cracks,  
488 contamination and wrinkles via controllable conformal contact, *Nat. Commun.*, 2022, **13**,  
489 4409.
- 490 [33] Y. Yang, J. Ma, Q. X. Pei, J. Yang, Y. Zhang, Cross-plane thermal transport in multilayer  
491 graphene/h-BN van der Waals heterostructures: The role of interface morphology, *Int. J.*  
492 *Heat Mass Transf.*, 2023, **216**, 124558.
- 493 [34] J. Zhu, J. H. Park, S. A. Vitale, W. Ge, G. S. Jung, J. Wang, M. Mohamed, T. Zhang, M.  
494 Ashok, M. Xue, X. Zheng, Z. Wang, J. Hansryd, A. P. Chandrakasan, J. Kong, T. Palacios,  
495 Low-thermal-budget synthesis of monolayer molybdenum disulfide for silicon back-end-of-  
496 line integration on a 200 mm platform, *Nat. Nanotechnol.*, 2023, **18**, 456–463.



- 497 [35] M. Yue, K. Zhang, M. Zhao, Y. Wang, D. Li, J. Liang, B. Zheng, C. Zou, Y. Ye, P. Wang,  
498 L. Zhang, S. Wang, 2D Cd metal contacts via low-temperature van der Waals epitaxy  
499 towards high-performance 2D transistors, *Nat. Commun.*, 2025, **16**, 4018.
- 500 [36] Y. Zhang, Z. Zhang, Y. Cheng, F. Cheng, L. Wang, N. Liu, L. Li, J. Su, Y. Gao, In situ TEM  
501 observation of controlled growth of two-dimensional WS<sub>2</sub> with vertically aligned layers and  
502 high-temperature stability, *Nano Energy*, 2020, **67**, 104221.
- 503 [37] C. Liu, Y. Jiang, B. Shen, S. Yuan, Z. Cao, Z. Bi, C. Wang, Y. Xiang, T. Wang, H. Wu, Z.  
504 Liu, Y. Wang, S. Wang, P. Zhou, A full-featured 2D flash chip enabled by system integration,  
505 *Nature*, 2025, 1–8.
- 506 [38] J. Chen, Y. Guo, Y. Su, K. Du, J. Jiang, Interface interaction, design, modulation, and  
507 optimization of van der Waals two-dimensional materials, *Mater. Today Phys.*, 2025, **58**,  
508 101878.
- 509 [39] Y. Xia, X. Chen, J. Wei, S. Wang, S. Chen, S. Wu, M. Ji, Z. Sun, Z. Xu, W. Bao, P. Zhou,  
510 12-inch growth of uniform MoS<sub>2</sub> monolayer for integrated circuit manufacture, *Nat. Mater.*,  
511 2023, **22**, 1324–1331.
- 512 [40] H. Hinton, H. Jang, W. Wu, M. H. Lee, M. Seol, H. J. Shin, S. Park, D. Ham, A 200×256  
513 image sensor heterogeneously integrating a 2D nanomaterial-based photo-FET array and  
514 CMOS time-to-digital converters, *ISSCC*, 2022, **pp.** 1–3.
- 515 [41] A. Quellmalz, X. Wang, S. Sawallich, B. Uzlu, M. Otto, S. Wagner, Z. Wang, M. Prechtl,  
516 O. Hartwig, S. Luo, G. S. Duesberg, M. C. Lemme, K. B. Gylfason, N. Roxhed, G. Stemme,  
517 F. Niklaus, Large-area integration of two-dimensional materials and their heterostructures  
518 by wafer bonding, *Nat. Commun.*, 2021, **12**, 917.
- 519 [42] V. K. Sangwan, D. Jariwala, I. S. Kim, K. S. Chen, T. J. Marks, L. J. Lauhon, M. C. Hersam,  
520 Gate-tunable memristive phenomena mediated by grain boundaries in single-layer MoS<sub>2</sub>,  
521 *Nat. Nanotechnol.*, 2015, **10**, 403–406.
- 522 [43] D. J. Late, B. Liu, H. S. S. Ramakrishna Matte, V. P. Dravid, C. N. R. Rao, Hysteresis in  
523 single-layer MoS<sub>2</sub> field effect transistors, *ACS Nano*, 2012, **6**, 5635–5641.
- 524 [44] S. G. Seo, S. H. Jin, Bias temperature stress instability of multilayered MoS<sub>2</sub> field-effect  
525 transistors with CYTOP passivation, *IEEE Trans. Electron Dev.*, 2019, **66**, 2208–2213.



- 526 [45] E. J. G. Santos, E. Kaxiras, Electrically driven tuning of the dielectric constant in  $\text{MoS}_2$  layers, View Article Online  
DOI: 10.1039/C3NR05332C  
527 *ACS Nano*, 2013, **7**, 10741–10746.
- 528 [46] E. J. G. Santos, E. Kaxiras, Electric-field dependence of the effective dielectric constant in  
529 graphene, *Nano Lett.*, 2013, **13**, 898–902.



The data that support the findings of this study are available from the corresponding author upon reasonable request.

